Validation of a Large-Scale Simulated Brightness Temperature Dataset Using SEVIRI Satellite Observations

JASON A. OTKIN, THOMAS J. GREENWALD, JUSTIN SIEGLAFF, AND HUNG-LUNG HUANG

Cooperative Institute for Meteorological Satellite Studies, University of Wisconsin—Madison, Madison, Wisconsin

(Manuscript received 4 November 2008, in final form 10 February 2009)

ABSTRACT

In this study, the accuracy of a simulated infrared brightness temperature dataset derived from a unique large-scale, high-resolution Weather Research and Forecasting (WRF) Model simulation is evaluated through a comparison with Spinning Enhanced Visible and Infrared Imager (SEVIRI) observations. Overall, the analysis revealed that the simulated brightness temperatures realistically depict many of the observed features, although several large discrepancies were also identified. The similar shapes of the simulated and observed probability distributions calculated for each infrared band indicate that the model simulation realistically depicted the cloud morphology and relative proportion of clear and cloudy pixels. A traditional error analysis showed that the largest model errors occurred over central Africa because of a general mismatch in the locations of deep tropical convection and intervening regions of clear skies and low-level cloud cover. A detailed inspection of instantaneous brightness temperature difference (BTD) imagery showed that the modeling system realistically depicted the radiative properties associated with various cloud types. For instance, thin cirrus clouds along the edges of deep tropical convection and within midlatitude cloud shields were characterized by much larger 10.8 − 12.0-μm BTD than optically thicker clouds. Simulated ice clouds were effectively discriminated from liquid clouds and clear pixels by the close relationship between positive 8.7 − 10.8-μm BTD and the coldest 10.8-μm brightness temperatures. Comparison of the simulated and observed BTD probability distributions revealed that the liquid and mixed-phase cloud-top properties were consistent with the observations, whereas the narrower BTD distributions for the colder 10.8-μm brightness temperatures indicated that the microphysics scheme was unable to simulate the full dynamic range of ice clouds.

1. Introduction

In recent years, proxy top-of-atmosphere (TOA) radiance datasets derived from numerical weather prediction (NWP) model output have been used to demonstrate the advanced measurement capabilities of future satellite sensors (e.g., Otkin et al. 2007). Such datasets are an attractive alternative to those derived from existing air- and ground-based instruments because they can easily be configured to represent the appropriate spatial, temporal, and spectral resolutions of the advanced sensor. A proxy dataset is most useful for demonstration purposes if it contains a realistic distribution of clear and cloudy pixels and a proper representation of all cloud types, across a large geographic domain or during a long time period. Satisfaction of this requirement is contingent upon the ability of the NWP model to accurately simulate cloud morphology and the evolution of the atmospheric state, which is at least partially dependent upon the availability of accurate initial conditions. Improved modeling of subgrid-scale processes, such as the complex interactions that occur between different hydrometeor species, and access to high-performance supercomputing resources have made this goal more attainable in recent years, particularly for memory-intensive simulations covering regional or hemispherical domains with high spatial resolution.

Upon completion of a model simulation, a forward radiative transfer model is used to convert the simulated temperature, moisture, and cloud fields into TOA radiances for each spectral band in a given sensor. The generation of realistic radiances for both clear and cloudy conditions is dependent upon the ability of the forward model to properly represent surface emission and reflection, gas absorption, and scattering by aerosols and cloud particles (e.g., Greenwald et al. 2002). Simulated clear-sky infrared radiances are generally very accurate

Corresponding author address: Jason A. Otkin, 1225 W. Dayton St., Madison, WI 53706.
E-mail: jason.otkin@ssec.wisc.edu

DOI: 10.1175/2009JAMC2142.1

© 2009 American Meteorological Society

(e.g., Derber and Wu 1998), although larger errors are expected to occur for simulated cloudy-sky radiances because of greater uncertainties in cloud scattering properties and in the treatment of mixed-phase clouds.

At the Cooperative Institute for Meteorological Satellite Studies (CIMSS) at the University of Wisconsin—Madison, significant effort in recent years has been directed toward demonstrating the measurement capabilities of the Advanced Baseline Imager (ABI) to be launched on the Geostationary Operational Environmental Satellite (GOES)-R in 2016 (Schmit et al. 2005). The high spatial and temporal resolution of the ABI in a geosynchronous orbit will provide unprecedented observational capabilities across the Western Hemisphere. The ongoing CIMSS effort involves the demonstration of various satellite retrieval algorithms, such as those for atmospheric motion vectors, water vapor and temperature soundings, and cloud properties, for different atmospheric conditions, as well as an evaluation of the algorithm performance for different measurement error assumptions. Performing these tasks in a realistic manner, however, requires the generation of proxy TOA radiance datasets with the correct ABI sensor specifications, which can only be accomplished through the use of high-resolution NWP model simulations and a forward radiative transfer model. To support this work, the CIMSS GOES-R proxy data team has produced several proxy ABI radiance datasets derived from large-scale Weather Research and Forecasting Model (WRF) simulations. Although the primary goal of the proxy data project is to simply provide physically realistic radiance datasets that are consistent with the observed atmospheric state, it is still important to determine the overall accuracy of the proxy datasets and to identify any biases or major sources of error that could negatively impact the retrieval algorithms. Because existing satellite observations suitable for evaluating the accuracy of proxy infrared radiances are somewhat limited over the proposed GOES-R viewing domain, a hemispheric-scale WRF simulation was performed over the Meteosat Second Generation (MSG) viewing area to use calibrated observations with high spatial and temporal resolution from the Spinning Enhanced Visible and Infrared Imager (SEVIRI). This simulation was performed on a high-performance supercomputer at the National Center for Supercomputing Applications (NCSA) at the University of Illinois at Urbana–Champaign.

Many prior studies have used satellite data to evaluate different aspects of NWP model performance. For instance, satellite data have been used to identify parameter sensitivities in a model's microphysics scheme (Zhang et al. 2001; Chaboureau et al. 2002; Keil et al. 2003; Chaboureau and Pinty 2006), to evaluate the accuracy of simulated cloud fields (Westphal et al. 1996; Yu et al. 1996; Garand and Nadon 1998; Klein and Jakob 1999; Mathieu et al. 1999; Chaboureau et al. 2000; Norris and Weaver 2001; Otkin and Greenwald 2008), and to validate operational forecast and climate models (Karlsson 1996; Rikus 1997; Tselioudis and Jakob 2002; Lopez et al. 2003; Sun and Rikus 2004). Overall, these studies have demonstrated the benefits of using satellite observations and a model-to-satellite approach to validate numerical model output.

In this study, the accuracy of a simulated infrared brightness temperature dataset derived from a high-resolution WRF simulation will be evaluated through a comparison with SEVIRI observations. An evaluation based on infrared brightness temperatures also provides a useful measure of the ability of a numerical model to realistically simulate cloud-top properties and the evolution of the temperature and water vapor fields. The primary focus of this study will be to examine the bulk characteristics of the simulated data aggregated across the entire domain. The paper is organized as follows: The WRF configuration and the simulated and observed SEVIRI brightness temperature datasets are described in section 2. Results are shown in section 3. Conclusions are presented in section 4.

2. Datasets and method

a. SEVIRI observations

Flying on the MSG geosynchronous satellite platform, SEVIRI provides high-quality measurements across 12 visible and infrared spectral bands (Schmetz et al. 2002). Except for a single broadband visible channel with 1-km horizontal resolution, the resolution of each channel is nominally 3 km at nadir, which is sufficient to observe mesoscale cloud, moisture, and surface temperature features. For this study, brightness temperature data from seven infrared channels (Table 1) will be used to examine the accuracy of the model-derived proxy dataset. The 6.2- and 7.3-μm channels are most sensitive to the water vapor content in the upper and midtroposphere, respectively, and the 8.7-, 10.8-, and 12.0-μm "window" channels are used to observe the surface and cloud-top temperatures. The 9.7-μm channel lies within the ozone absorption band but can also be used to monitor features along the tropopause and within the lower stratosphere. The 13.4-μm channel lies within a carbon dioxide absorption band and can be used for cloud height assignment and cirrus discrimination.

b. WRF description

The WRF is a sophisticated NWP model that solves the compressible nonhydrostatic Euler equations cast in

TABLE 1. SEVIRI band number, central wavelength, and primary use.

Band no.	Central wavelength (μm)	Primary use
5	6.2	Upper-level water vapor
6	7.3	Midlevel water vapor
7	8.7	Cloud and surface temperatures
8	9.7	Ozone and upper-level features
9	10.8	Cloud and surface temperatures
10	12.0	Cloud and surface temperatures
11	13.4	Cirrus discrimination and cloud-top pressure estimates

flux form on a mass-based terrain-following vertical coordinate system. Prognostic variables include the horizontal and vertical wind components, various microphysical quantities, and the perturbation potential temperature, geopotential, and surface pressure of dry air. High-resolution global datasets are used to initialize the model topography and other static surface fields. A complete description of the WRF modeling system is contained in Skamarock et al. (2005).

Version 2.2 of the WRF was used for this study. The simulation was initialized at 1800 UTC 15 August 2006 using 1° Global Data Assimilation System analyses and then integrated for 30 h on a single 5950 × 5420 gridpoint domain (Fig. 1) covering ~38% of the earth's surface with 3-km horizontal grid spacing and 52 vertical levels. The vertical resolution decreased from less than 100 m in the lowest kilometer to ~625 m at the model top, which was set to 28 hPa. This massive simulation required approximately 1.5 terabytes (TB) of physical memory and 87 000 CPU hours to complete. Subgrid-scale processes were parameterized using the Thompson et al. (2008) mixed-phase cloud microphysics scheme, the Mellor–Yamada–Janjic planetary boundary layer scheme (Mellor and Yamada 1982), and the Dudhia (1989) shortwave and Rapid Radiative Transfer Model (Mlawer et al. 1997) longwave radiation schemes. Surface heat and moisture fluxes were calculated using the National Centers for Environmental Prediction–Oregon State University–Air Force–Hydrologic Research Laboratory (Noah) land surface model. No cumulus parameterization scheme was used; therefore, all clouds were explicitly predicted by the microphysics scheme.

c. *Forward model description*

The radiance calculation for each SEVIRI infrared channel involves several steps within the forward modeling system. First, "CompactOPTRAN," which is part of the National Oceanic and Atmospheric Administration Community Radiative Transfer Model (CRTM), is used to compute gas optical depths for each model layer from the WRF-simulated temperature and water vapor mixing ratio profiles and climatological ozone data. Ice cloud absorption and scattering properties, such as extinction efficiency, single-scatter albedo, and full scattering

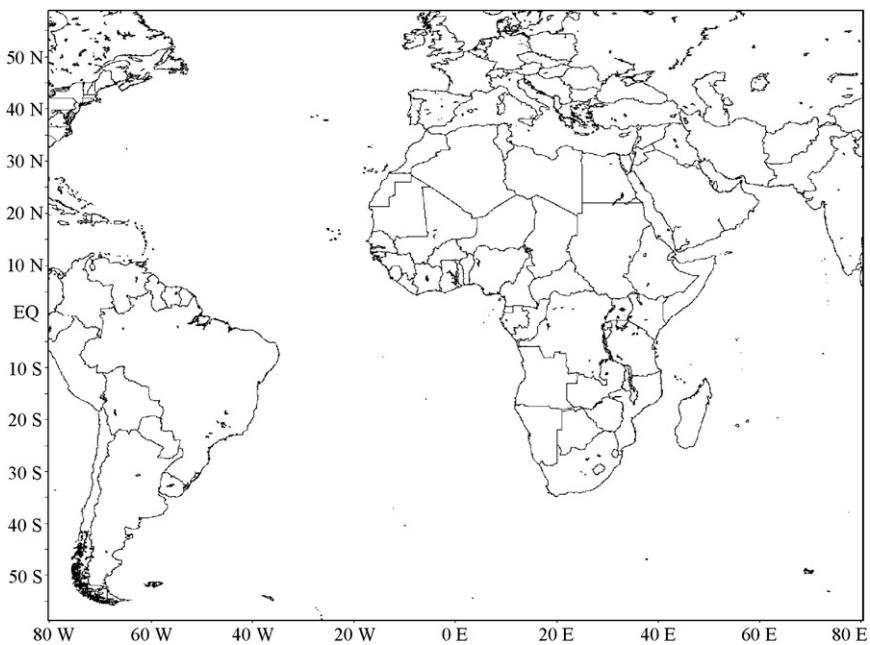

FIG. 1. Geographical region covered by the 5950 × 5420 gridpoint domain with 3-km horizontal grid spacing.

phase function, obtained from Baum et al. (2005) are subsequently applied to each frozen hydrometeor species (i.e., ice, snow, and graupel) predicted by the microphysics parameterization scheme. A lookup table based on Lorenz–Mie calculations is used to assign the properties for the cloud water and rainwater species. Visible cloud optical depths are calculated separately for the liquid and frozen hydrometeor species by following the work of Han et al. (1995) and Heymsfield et al. (2003), respectively, and then are converted into infrared cloud optical depths by scaling the visible optical depths by the ratio of the corresponding extinction efficiencies. The longer pathlength for zenith angles >0 is accounted for by scaling the optical depth by the inverse of the cosine of the zenith angle. The surface emissivity over land was obtained from the Seeman et al. (2008) global emissivity dataset, whereas the water surface emissivity was computed using the CRTM Infrared Sea Surface Emissivity Model. Last, the simulated skin temperature and atmospheric temperature profiles, along with the layer gas optical depths and cloud scattering properties, were input to the successive-order-of-interaction (SOI) forward radiative transfer model (Heidinger et al. 2006) to generate simulated TOA radiances for each SEVIRI infrared band.

After an initial 6-h spinup period, radiances were calculated across the entire domain every 30 min during the remaining 24 h of the simulation. To produce a more representative proxy dataset containing the correct spatial sampling at all satellite zenith angles, the simulated radiances were remapped from the WRF projection to the geosynchronous SEVIRI projection using a weighted average of all of the simulated grid boxes overlapping a given SEVIRI observation box. Given that the satellite resolution decreases with increasing zenith angle whereas the WRF grid maintains a constant 3-km horizontal resolution across the entire domain, this step will slightly coarsen the resolution of the simulated radiance dataset. The remapped radiances were converted into brightness temperatures using the Planck function and the CompactOPTRAN polychromatic corrections.

3. Results

a. Case study description

This section begins with a brief overview of the observed and simulated large-scale conditions that occurred during the case study. The 8.7-μm brightness temperature data will be used for this analysis because they provide a convenient means to observe both surface and cloud features. Given the size of the domain, only a few of the more salient features will be discussed here. At 0000 UTC 16 August 2006 (Figs. 2a,b), a nearly continuous line of cloud cover with embedded regions of deep convection extended from the northern end of South America eastward across the Atlantic Ocean and most of Africa. The localized regions of deep convection in the simulation were generally too far to the west, with the greatest activity occurring over central Africa rather than over the Rift Valley farther to the east. Cloud features over the midlatitude regions were generally well simulated, with several areas of cirrus and deep convection embedded within a large region of cloud cover over the North Atlantic and Europe. The southern midlatitudes were also characterized by extensive cloud cover with several distinct areas of enhanced upper-level cloudiness located along a very strong jet stream that extended across much of the southern portion of the domain. Several large areas of clear skies were located across portions of the subtropical North and South Atlantic; most of northern Africa, the eastern Mediterranean, and the Middle East; and much of South Africa and adjacent areas of the Atlantic and Indian Oceans. With the exception of the poor model depiction of the low-level cloud distribution over the South Atlantic, the size and location of each of these clear areas were generally correct.

By 1200 UTC (Figs. 2c,d), the model simulation continued to depict realistically the overall structure and evolution of the cloud fields associated with the various midlatitude disturbances. Large discrepancies continued to occur across the South Atlantic, however, where the simulated boundary layer clouds were generally too small and lacked the large-scale organization found in the observations. The relatively warm cloud-top brightness temperatures suggest that the PBL scheme contained insufficient vertical mixing across this region, which prevented the cloud-topped boundary layer from reaching its proper depth. It is also possible that the absence of smoke and aerosol particles in the model resulted in an incorrect specification of the cloud condensation nuclei concentration downwind of the large biomass burning regions over equatorial Africa, which may have led to the development of optically thinner clouds characterized by lower (i.e., warmer) effective cloud-top heights. Strong daytime heating had substantially warmed the surface temperatures within the clear-sky regions over Africa and the Middle East. The tendency for the simulated brightness temperatures to be slightly cooler than observed, however, indicates that the simulated diurnal cycle is too small.

By 0000 UTC 17 August (Figs. 2e,f), many of the same large-scale patterns were still evident across the

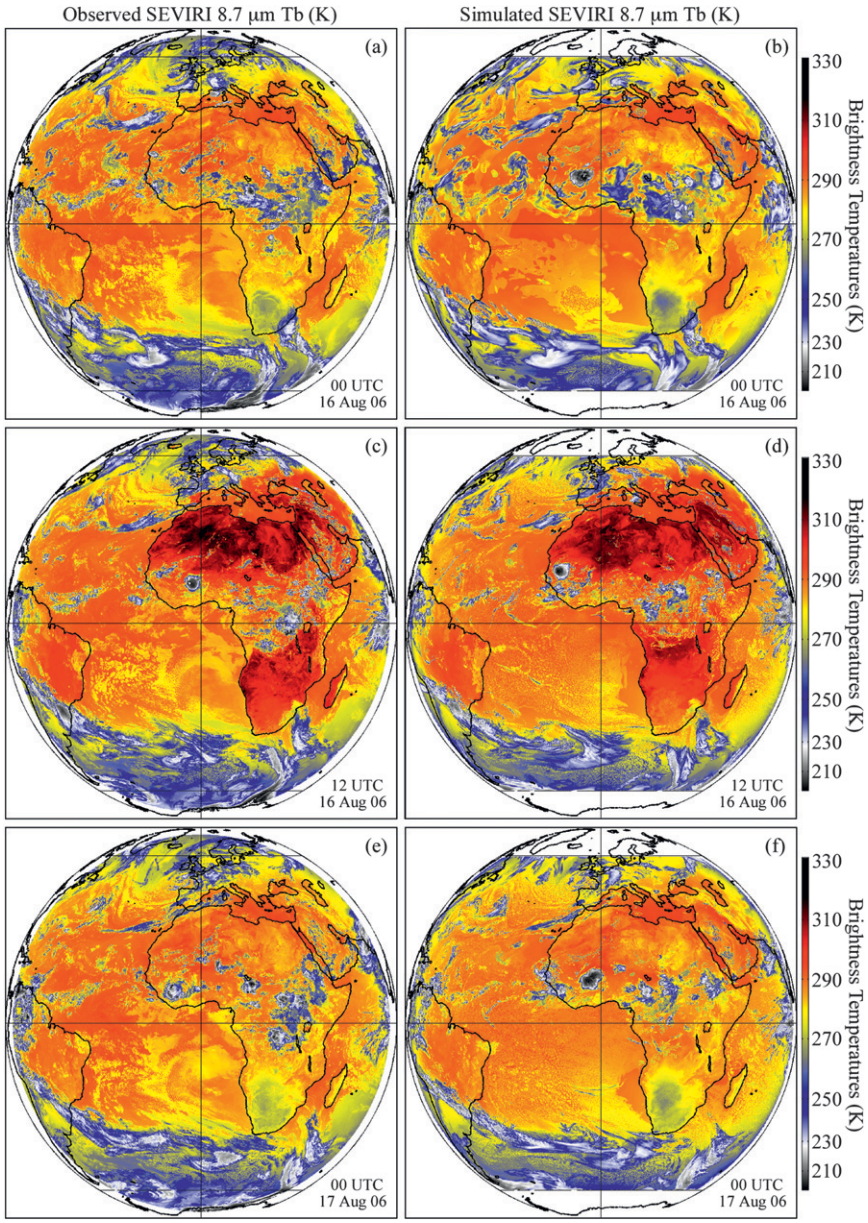

FIG. 2. SEVIRI 8.7-μm brightness temperatures (K) valid at (a) 0000 UTC 16 Aug 2006, (c) 1200 UTC 16 Aug 2006, and (e) 0000 UTC 17 Aug 2006. Simulated SEVIRI 8.7-μm brightness temperatures (K) valid at (b) 0000 UTC 16 Aug 2006, (d) 1200 UTC 16 Aug 2006, and (f) 0000 UTC 17 Aug 2006.

model domain. Overall, the simulated brightness temperatures continued to realistically depict most of the midlatitude cloud features, albeit with greater displacement errors; the most substantial large-scale errors were present over central Africa. Although this region was characterized by a basic mismatch in the locations of the deep convection and clear areas, it is evident that the simulation still sampled the full distribution of clear and cloudy pixels across this region.

b. *Diurnal cycle*

To examine the temporal evolution of each channel in greater detail, time series of the mean simulated and observed brightness temperatures for all grid points with a zenith angle of less than 70° are shown in Fig. 3. As expected, the largest diurnal cycles occur for the 8.7-, 10.8-, and 12.0-μm window channels because they are most sensitive to the large changes that occur in the

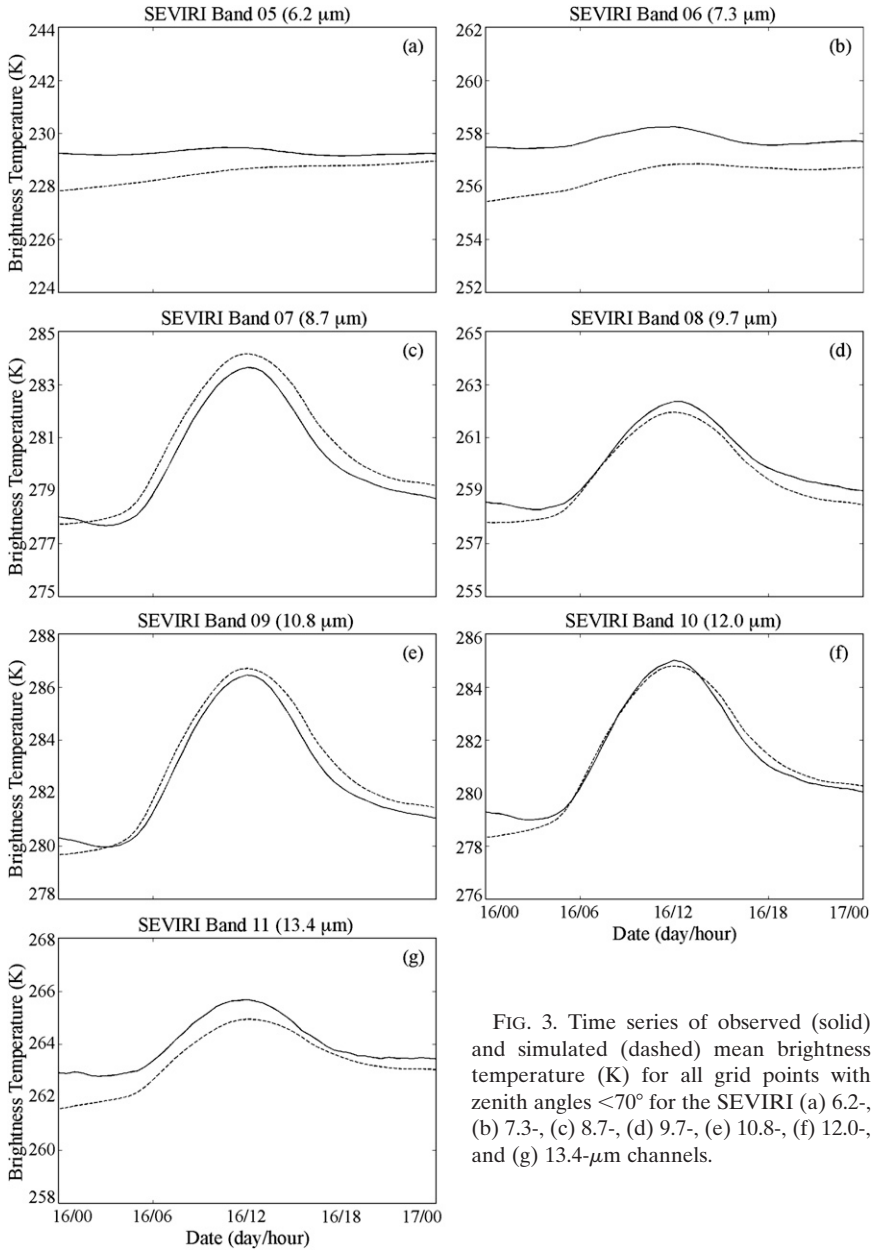

FIG. 3. Time series of observed (solid) and simulated (dashed) mean brightness temperature (K) for all grid points with zenith angles <70° for the SEVIRI (a) 6.2-, (b) 7.3-, (c) 8.7-, (d) 9.7-, (e) 10.8-, (f) 12.0-, and (g) 13.4-μm channels.

surface temperature each day. The 6.2- and 7.3-μm water vapor channels are characterized by the flattest diurnal cycles because the upper-level water vapor content typically does not change quickly over such a large domain. Except for the first few hours, the simulated brightness temperatures closely follow the observed diurnal cycle with little or no time lag, which indicates that the WRF realistically simulated the daily range in surface temperatures and cloud cover across the domain. The initial departure from the observed diurnal cycle is likely an artifact of the model spinup process and could possibly have been avoided through the use of a higher-resolution initialization dataset. The mean bias error is generally very small for each channel (Table 2) and, with the exception of the water vapor channels, does not vary much during the simulation. The small warm bias in the window channels suggests that the simulation may contain fewer upper-level clouds than were observed. Though not examined in this paper, the relatively large cold bias for each water vapor channel appears to be due to a model initialization error that resulted in excessive water vapor content in the upper troposphere. This bias causes the signal for the synthetic brightness temperatures to peak at a higher

TABLE 2. Brightness temperature bias (K) during the 24-h period.

Band no.	Central wavelength (μm)	Bias (K)
5	6.2	−0.76
6	7.3	−1.35
7	8.7	0.53
8	9.7	−0.40
9	10.8	0.32
10	12.0	−0.01
11	13.4	−0.64

(i.e., colder) atmospheric level because of enhanced water vapor absorption. The tendency for the negative bias to decrease with time suggests that the microphysics scheme may be slowly removing the excess water vapor during the simulation.

c. *Probability distributions*

Figure 4 shows the simulated and observed probability distributions for all times and locations with a zenith angle that is less than 70°. Aside from differences in the small-scale details, the overall shapes of the simulated distributions are remarkably consistent with the corresponding observations. Given the strong sensitivity of infrared brightness temperatures to both the horizontal and vertical extent of the cloud field, the similar distributions suggest that the parameterization schemes in the WRF were able to simulate realistically the cloud morphology and the relative proportion of clear and cloudy pixels. Although local differences in the simulated cloud field are certainly evident in Fig. 2, the general agreement between the distributions indicates that the model simulation contains a representative sample of the cloud types that occurred during this case study. The similar shape of the ''cold'' tail in each distribution lends additional support to these conclusions.

d. *Statistical error analysis*

Although the excellent agreement between the simulated and observed brightness temperature distributions clearly satisfies the goal of producing a realistic proxy dataset, it is still important to examine the horizontal structure of the proxy data and its associated error statistics. In Fig. 5, the mean observed and simulated brightness temperatures and mean absolute error averaged over the 24-h period are shown for three channels that are sensitive to different layers of the atmosphere. Comparison of the mean brightness temperature fields reveals that the horizontal structure and magnitude of the simulated data closely match the observations within the subtropical and midlatitude regions. For instance, the simulated data realistically depict the complex upper-level cloud pattern that developed along and to the south of the southern midlatitude jet stream as well as the clouds associated with the large extratropical cyclone over northern Europe. Much larger discrepancies, however, occurred across central Africa because of the large westward displacement of the tropical waves and associated deep convection across this region. Inspection of the mean absolute error data shows that each channel is characterized by a similar error pattern, with the largest errors occurring for the 10.8-μm window channel because it is most sensitive to errors in the upper-level cloud distribution. As expected, the largest errors were located across central Africa, because the localized nature of the deep convection could potentially produce brightness temperature errors in excess of 100 K if the other dataset only contained clear or low-level clouds. Much smaller errors were present across the subtropical South Atlantic and the various clear-sky regions identified in Fig. 2. Even though the clouds were generally well simulated over the midlatitude regions, small phase errors and the limited predictability of the individual convective clouds within these regions resulted in relatively large errors, which illustrates the difficulty of applying standard statistical measures to evaluate the accuracy of high-resolution model datasets containing heterogeneous cloud fields. Note, however, that these small-scale errors are generally unimportant when producing a proxy satellite dataset as long as the overall cloud features are realistic.

To eliminate the sensitivity to differences in the cloud distribution, error statistics were calculated for pixels that were identified as clear in both datasets by an infrared-only cloud mask algorithm. Approximately 28% of the pixels with a zenith angle that is less than 70° satisfied this requirement, with a majority of the pixels occurring over land. Overall, the simulated clear-sky brightness temperatures are characterized by a mean error <2.5 K for each channel (Table 3). O'Dell et al. (2006) have shown that the SOI model is accurate to within 1 K at microwave wavelengths for a full range of atmospheric conditions, which suggests that most of the errors in the simulated data are caused by other components of the modeling system, such as the surface emissivity or the simulated temperature and water vapor fields. For instance, removal of the negative temperature bias caused by the excessive upper-level water vapor content would greatly improve the accuracy of the clear-sky brightness temperatures.

e. *Brightness temperature differences*

In the remainder of this section, the accuracy of the proxy dataset will be further assessed through a detailed

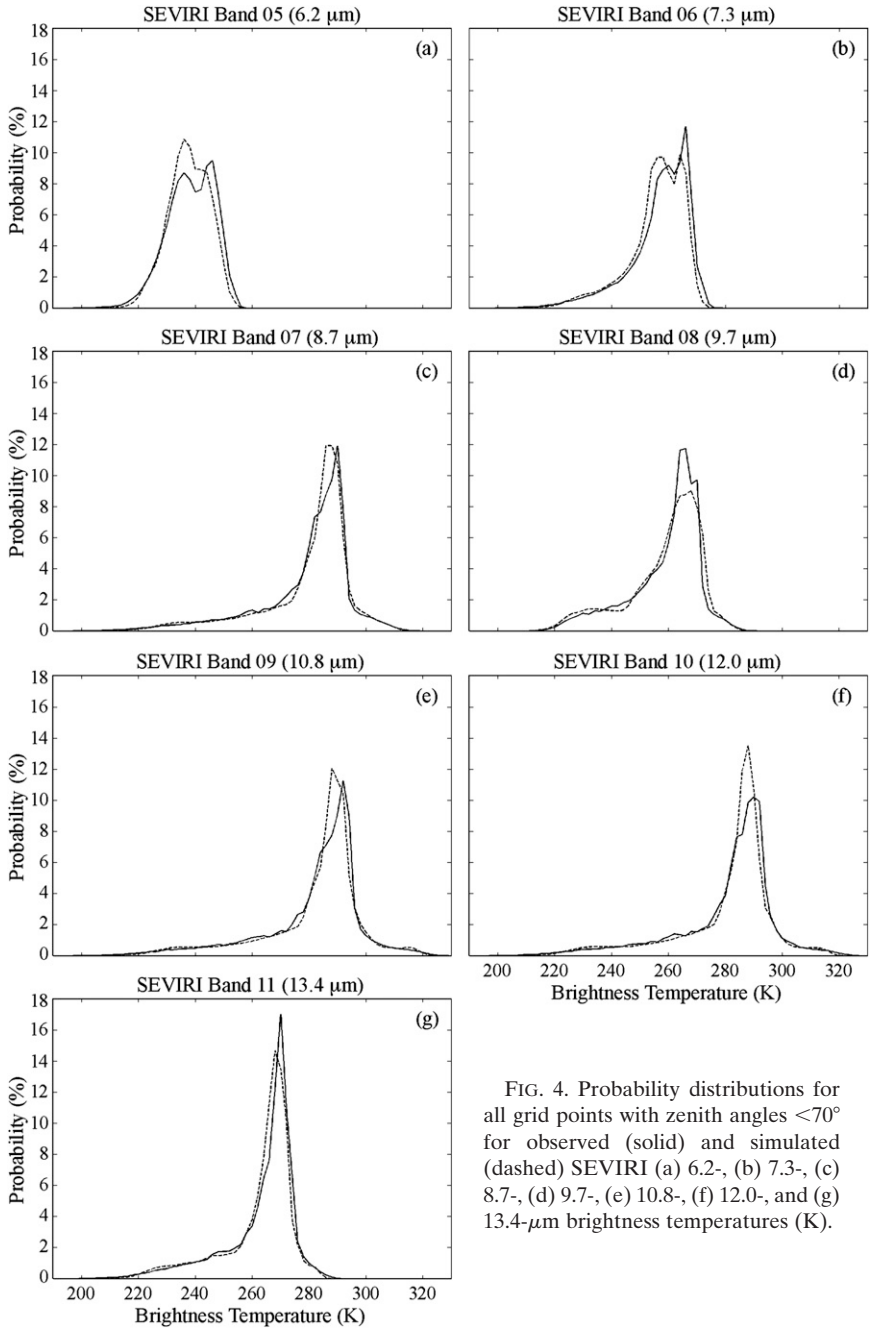

FIG. 4. Probability distributions for all grid points with zenith angles <70° for observed (solid) and simulated (dashed) SEVIRI (a) 6.2-, (b) 7.3-, (c) 8.7-, (d) 9.7-, (e) 10.8-, (f) 12.0-, and (g) 13.4-μm brightness temperatures (K).

examination of the brightness temperature differences (BTD) calculated for several infrared channel combinations. The BTD technique is widely used to infer cloud properties and the presence of trace atmospheric constituents, such as dust and volcanic ash. Figure 6 shows a representative example of the simulated and observed 10.8-μm brightness temperatures and the 10.8 − 12.0- and 8.7 − 10.8-μm BTD for all pixels with a zenith angle that is less than 70°. A qualitative comparison of the images reveals that the simulated BTD realistically depict many of the observed features. For instance, greater water vapor absorption at 12.0 μm causes the 10.8 − 12.0-μm BTD to be positive in most regions, with the largest values occurring over the tropics where significant low-level moisture is present. Additional elongated and circular bands of large positive BTD associated with thin cirrus clouds are located over central Africa, the North Atlantic, and the southern midlatitude regions. These clouds are indicated by the slightly warmer 10.8-μm brightness temperatures

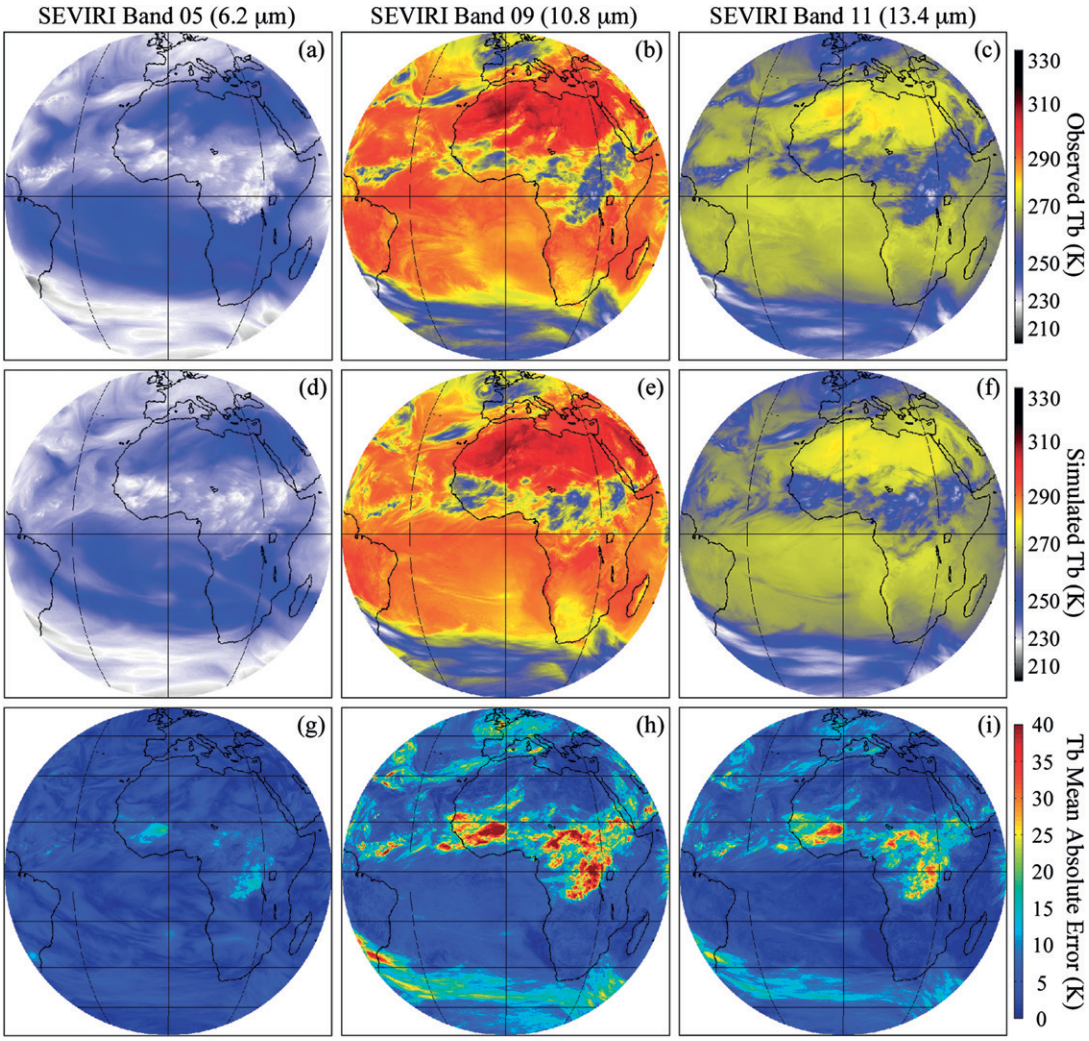

FIG. 5. Mean SEVIRI (a) 6.2-, (b) 10.8-, and (c) 13.4-μm brightness temperatures (K). Mean simulated SEVIRI (d) 6.2-, (e) 10.8-, and (f) 13.4-μm brightness temperatures (K). Mean absolute error (K) for simulated (g) 6.2-, (h) 10.8-, and (i) 13.4-μm brightness temperatures.

surrounding the deep tropical convection and the midlatitude cloud shields. Prabhakara et al. (1988) have shown that thin cirrus clouds are characterized by large BTD that is due to the enhanced extinction of radiation by small ice particles at 12.0 μm. Based on the 10.8-μm imagery, BTDs between 1 and 2 K over the tropics correspond to regions with high water vapor content and little or no cloud cover while BTD values >2 K are primarily associated with thin cirrus clouds. The deeper convective clouds across this region contain smaller BTD because the larger ice particles near the cloud top cause the weighting functions for both channels to peak near the same level, thereby resulting in similar brightness temperatures and a small BTD. Large areas of negative BTD values are primarily limited to arid and semiarid locations, such as the Sahara and much of southern Africa. The large positive bias in the simulated BTD data over the western two-thirds of the Sahara is likely due to the lack of dust in the numerical model, which was important for this case since a significant dust

TABLE 3. Mean absolute error (K) and bias (K) for clear-sky simulated SEVIRI brightness temperatures.

Band no.	Central wavelength (μm)	Mean absolute error (K)	Bias (K)
5	6.2	2.50	−1.68
6	7.3	2.17	−1.79
7	8.7	2.34	−0.24
8	9.7	2.79	−0.99
9	10.8	2.44	−0.40
10	12.0	2.50	−0.99
11	13.4	1.71	−1.03

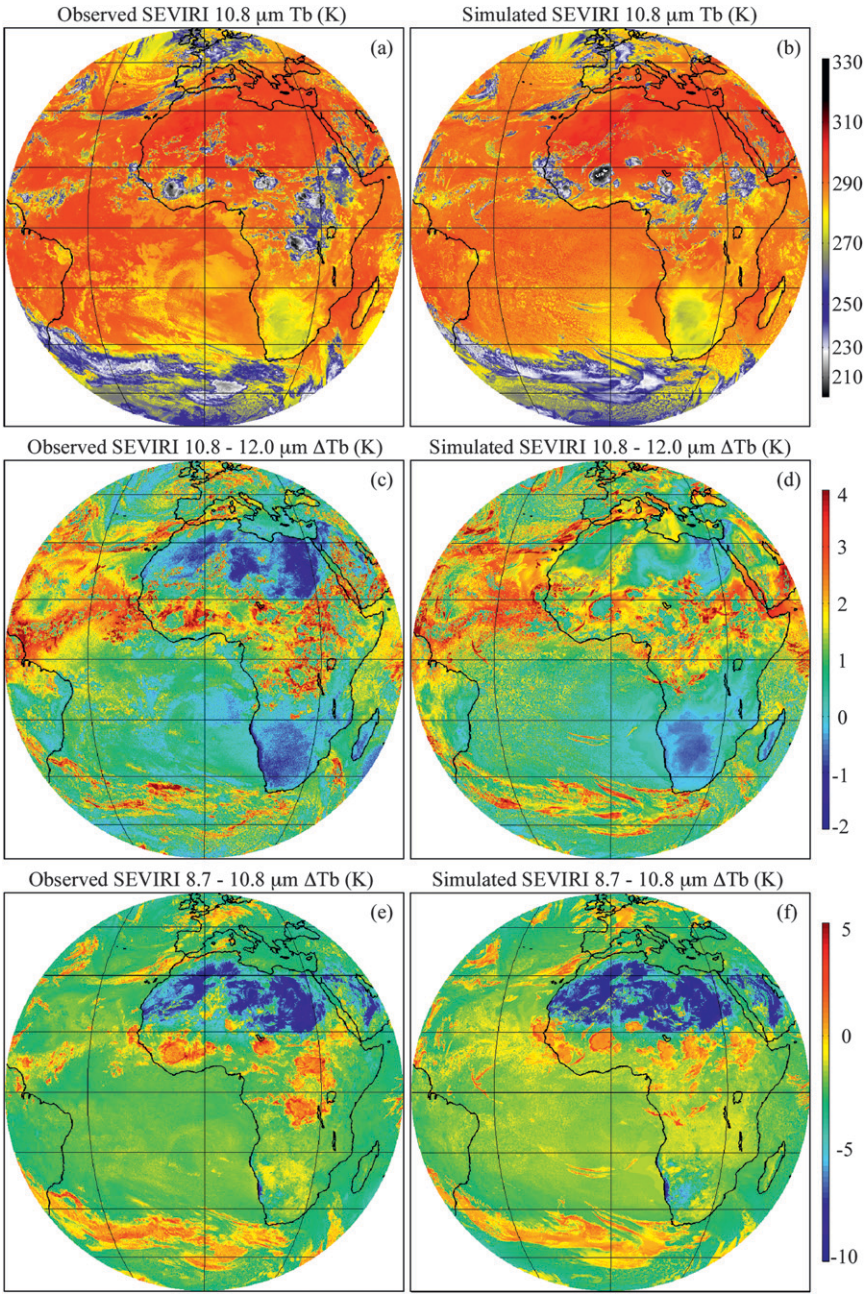

FIG. 6. (a) Observed and (b) simulated SEVIRI 10.8-μm brightness temperatures (K). (c) Observed and (d) simulated SEVIRI 10.8 − 12.0-μm brightness temperature differences (K). (e) Observed and (f) simulated SEVIRI 8.7 − 10.8-μm brightness temperature differences (K). All images are valid at 2200 UTC 16 Aug 2006.

storm was ongoing across this region (Liu et al. 2008). A greater sensitivity to dust with a corresponding reduction in the brightness temperatures at 10.8 μm causes the negative BTD (Ackerman 1997).

The 8.7 − 10.8-μm BTD data can be used to effectively discriminate liquid and ice clouds because of differences in their radiative properties (Ackerman et al. 1990; Strabala et al. 1994; Baum et al. 2000). Near 8.7 μm, the imaginary part of the complex index of refraction, which is a measure of absorption for a given hydrometeor size distribution, is similar for both water and ice particles but is substantially larger for ice at 10.8 μm. In a typical case, ice clouds are characterized by a positive BTD while liquid clouds have a negative

BTD. This distinction is clearly illustrated in Fig. 6 by the close relationship between the positive BTD and the coldest 10.8-μm brightness temperatures across the entire domain. The realistic distribution of positive BTD in the simulated data indicates that the cloud properties produced by the Thompson microphysics scheme and the scattering and absorption properties used by the forward model are representative of those found in real clouds. Clear areas are generally characterized by negative BTDs in both datasets because of greater water vapor absorption at 8.7 μm. The largest negative BTDs occur over desert areas because of a lower surface emissivity at 8.7 μm than at 10.8 μm. Although errors in the prescribed emissivity and the greater sensitivity of the 8.7-μm brightness temperatures to the water vapor bias in the simulated data may have contributed to the larger negative BTDs across the Sahara, much of the discrepancy in this region is again most likely due to the lack of dust in the numerical model.

The simulated and observed BTD probability distributions for three different channel combinations are shown in Fig. 7. The distributions contain data from all locations with a zenith angle that is less than 70°. Because of strong water vapor absorption at 6.2 μm and a general decrease in temperature with height in the troposphere, the 6.2 − 10.8-μm BTD is usually negative, with the largest differences occurring for clear regions containing abundant moisture and high surface temperatures. The similar shape of each distribution indicates that the numerical model realistically simulated the cloud-top height, because large height errors would result in very different BTD distributions. The positive BTD pixels occurring for the coldest 10.8-μm brightness temperatures correspond to overshooting cloud tops within regions of deep convection, particularly over central Africa. Chung et al. (2008) have shown that the positive BTD for such clouds result from greater water vapor emission at 6.2 μm associated with convectively generated moisture anomalies in the lower stratosphere. Inspection of the simulated 8.7 − 10.8- and 10.8 − 12.0-μm BTD distributions reveals a remarkable level of agreement with the observations, with both distributions exhibiting the familiar ''arch'' pattern first described by Inoue (1987) and Strabala et al. (1994). Although the shape of each simulated distribution is generally correct for the liquid and mixed-phase clouds, the narrower BTD distribution for colder 10.8-μm brightness temperatures indicates that the microphysics scheme is unable to simulate the full dynamic range of the ice clouds, which is not surprising given the tremendous complexity associated with modeling ice microphysical processes. The similar magnitude and similar location of the maximum probability bands extending across each distribution, however, indicate that most of the ice and liquid clouds are realistically simulated.

4. Conclusions

In this study, the accuracy of a unique large-scale, high-resolution WRF simulation was evaluated through a detailed comparison of simulated and observed SEVIRI infrared brightness temperatures. A sophisticated forward radiative transfer model capable of realistically treating complex radiative processes in both clear and cloudy conditions was used to convert the model-simulated temperature, moisture, and cloud fields into synthetic SEVIRI observations. The large geographic scope of the simulation provided a valuable opportunity to evaluate the performance of a particular suite of parameterization schemes over a diverse range of atmospheric conditions and to infer the accuracy of the NWP–forward modeling system used to generate synthetic satellite radiance datasets.

Overall, the analysis revealed that the simulated brightness temperatures realistically depicted many of the observed features, although several large discrepancies were also identified. Mean brightness temperatures calculated for each channel demonstrate that the simulated dataset contains a realistic diurnal cycle, with the largest (smallest) daily range occurring for the window (water vapor) channels. The similar shapes of the simulated and observed probability distributions indicate that the parameterization schemes realistically simulated the cloud morphology and relative proportion of clear and cloudy pixels. Excessive upper-level water vapor content due to an error in the model initialization contributed to larger negative brightness temperature biases in the nonwindow channels. A traditional error analysis showed that the largest errors occurred over central Africa because of a general mismatch in the locations of deep tropical convection and intervening regions of clear skies and low-level cloud cover. Even though the clouds were generally well simulated over the midlatitude regions, small location errors and the limited predictability of the small-scale clouds in these regions resulted in relatively large errors. Relatively small errors were present across the subtropical Atlantic, although the tendency for the simulated brightness temperatures to be too warm suggests that the PBL scheme produced insufficient vertical mixing across this region.

A detailed inspection of instantaneous BTD imagery showed that the modeling system realistically depicted the radiative properties associated with many of the cloud features. For instance, thin cirrus clouds along the edges of the deep tropical convection and within the

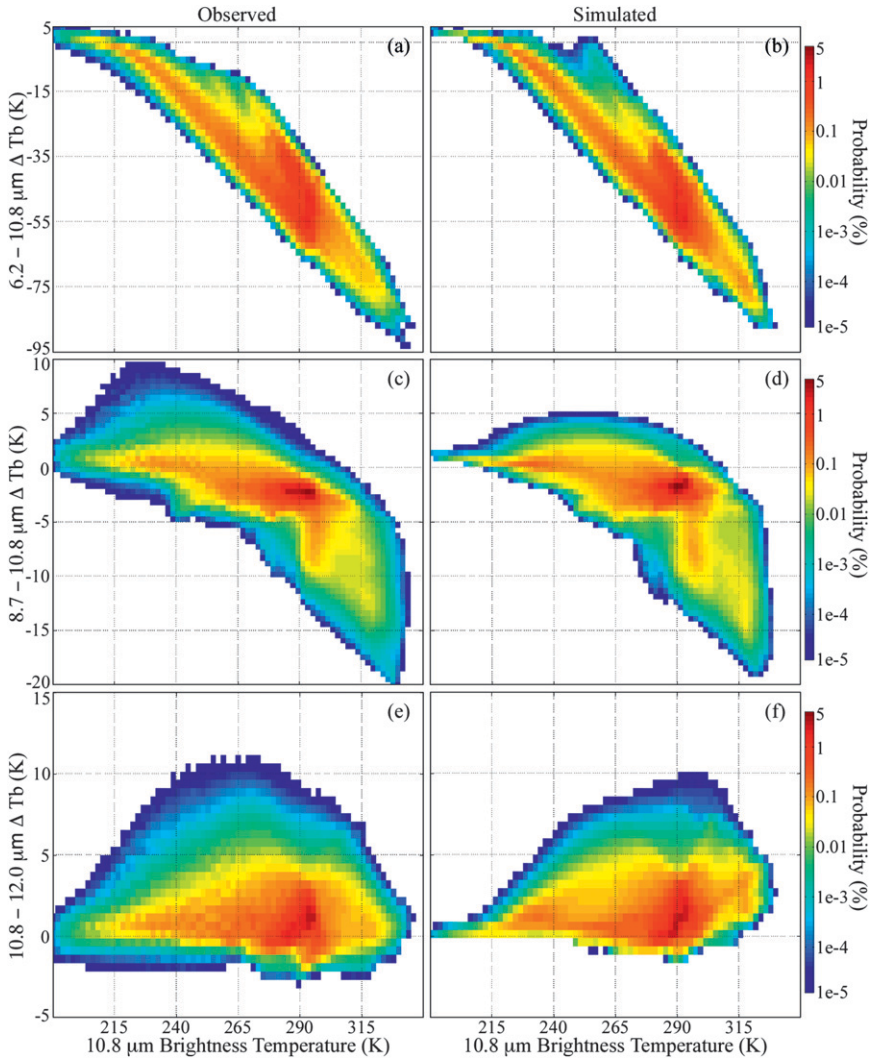

FIG. 7. Probability distributions for all grid points with a zenith angle <70° for (a) observed and (b) simulated SEVIRI 6.2 − 10.8-μm brightness temperature difference (K); (c) observed and (d) simulated SEVIRI 8.7 − 10.8-μm brightness temperature difference (K); (e) observed and (f) simulated SEVIRI 10.8 − 12.0-μm brightness temperature difference (K).

various midlatitude cloud shields were characterized by much larger 10.8 − 12.0-μm BTD than optically thicker clouds. Simulated ice clouds were effectively discriminated from liquid clouds and clear pixels by the close relationship between positive 8.7 − 10.8-μm BTD and the coldest 10.8-μm brightness temperatures. Comparison of the simulated and observed BTD probability distributions revealed that the liquid and mixed-phase cloud-top properties were consistent with the observations, whereas the narrower BTD distribution for the colder 10.8-μm brightness temperatures indicated that the microphysics scheme was unable to simulate the full dynamic range of the ice clouds. Large BTD errors also occurred over the western and central Sahara because of the lack of dust in the numerical model, which was important for this case because a significant dust storm was occurring across this region. This sensitivity illustrates the importance of including aerosols and other trace gases as input to the forward radiative transfer model.

As mentioned in the introduction, proxy satellite radiance datasets are currently being used at CIMSS to demonstrate future satellite retrieval algorithms and to evaluate algorithm performance for different measurement error assumptions. The model problems described above, such as the lack of very optically thin ice clouds, the poor representation of the marine boundary layer clouds over the Atlantic Ocean, and the absence of smoke, dust, and other aerosols in the model, represent

important departures from the real atmosphere that could adversely affect the demonstration of certain algorithms, particularly those that are sensitive to aerosols. Because of this strong sensitivity, air transport and chemistry models will be used to provide realistic aerosol information for future proxy radiance datasets. Errors in the cloud distribution will typically have the greatest impact on the cloud-top property retrieval algorithms, such as cloud phase and cloud optical depth. Even with these discrepancies, it is clear that the combined NWP–forward modeling system is able to produce proxy radiance datasets that realistically depict most of the cloud, temperature, and water vapor features observed in the real atmosphere and that are therefore useful for demonstration purposes.

Future work includes using *CloudSat* data to examine the vertical hydrometeor structure associated with various cloud regimes in the simulated data. Detailed studies employing infrared, microwave, and *CloudSat* data will also be undertaken to investigate more thoroughly the simulated cloud structure for certain cloud types, such as the stratocumulus clouds in the South Atlantic or the extensive cloud shields located in the midlatitude regions. Last, as our visible forward modeling capabilities mature, we plan to compare simulated and observed SEVIRI visible reflectances for this case study, which will provide additional information about the accuracy of the simulated cloud-top properties.

Acknowledgments. This work was funded under the National Oceanic and Atmospheric Administration Cooperative Agreement NA06NES4400002. Additional support was provided by the NCSA under Grant ATM060029. Special thanks are given to Gerardo Cisneros of Silicon Graphics, Inc., and to the NCSA personnel for their help with the WRF simulation, which was performed on the ''cobalt'' supercomputer. Comments from three anonymous reviewers helped to improve the manuscript.

REFERENCES

Ackerman, S. A., 1997: Remote sensing aerosols using satellite infrared observations. *J. Geophys. Res.,* **102,** 17 069–17 079.

——, W. L. Smith, J. D. Spinhirne, and H. E. Revercomb, 1990: The 27–28 October 1986 FIRE IFO Cirrus Case Study: Spectral properties of cirrus clouds in the 8–12 μm window. *Mon. Wea. Rev.,* **118,** 2377–2388.

Baum, B. A., P. F. Soulen, K. I. Strabala, M. D. King, S. A. Ackerman, W. P. Menzel, and P. Yang, 2000: Remote sensing of cloud properties using MODIS Airborne Simulator imagery during SUCCESS. II. Cloud thermodynamic phase. *J. Geophys. Res.,* **105,** 11 781–11 792.

——, P. Yang, A. J. Heymsfield, S. Platnick, M. D. King, Y.-X. Hu, and S. T. Bedka, 2005: Bulk scattering properties for the remote sensing of ice clouds. Part II: Narrowband models. *J. Appl. Meteor.,* **44,** 1896–1911.

Chaboureau, J.-P., and J.-P. Pinty, 2006: Validation of a cirrus parameterization with Meteosat Second Generation observations. *Geophys. Res. Lett.,* **33,** L03815, doi:10.1029/2005GL024725.

——, J.-P. Cammas, P. Mascart, J.-P. Pinty, C. Claud, R. Roca, and J.-J. Morcrette, 2000: Evaluation of a cloud system life-cycle simulated by Meso-NH during FASTEX using Meteosat radiances and TOVS-3I cloud retrievals. *Quart. J. Roy. Meteor. Soc.,* **126,** 1735–1750.

——, ——, P. J. Mascart, J.-P. Pinty, and J.-P. Lafore, 2002: Mesoscale model cloud scheme assessment using satellite observations. *J. Geophys. Res.,* **107,** 4301, doi:10.1029/2001JD000714.

Chung, E.-S., B.-J. Sohn, and J. Schmetz, 2008: *CloudSat* shedding new light on high-reaching tropical deep convection observed with Meteosat. *Geophys. Res. Lett.,* **35,** L02814, doi:10.1029/2007GL032516.

Derber, J. C., and W.-S. Wu, 1998: The use of TOVS cloud-cleared radiances in the NCEP SSI analysis system. *Mon. Wea. Rev.,* **126,** 2287–2299.

Dudhia, J., 1989: Numerical study of convection observed during the Winter Monsoon Experiment using a mesoscale two-dimensional model. *J. Atmos. Sci.,* **46,** 3077–3107.

Garand, L., and S. Nadon, 1998: High-resolution satellite analysis and model evaluation of clouds and radiation over the Mackenzie basin using AVHRR data. *J. Climate,* **11,** 1976–1996.

Greenwald, T. J., R. Hertenstein, and T. Vukicevic, 2002: An all-weather observational operator for radiance data assimilation with mesoscale forecast models. *Mon. Wea. Rev.,* **130,** 1882–1897.

Han, Q., W. Rossow, R. Welch, A. White, and J. Chou, 1995: Validation of satellite retrievals of cloud microphysics and liquid water path using observations from FIRE. *J. Atmos. Sci.,* **52,** 4183–4195.

Heidinger, A. K., C. O'Dell, R. Bennartz, and T. Greenwald, 2006: The successive-order-of-interaction radiative transfer model. Part I: Model development. *J. Appl. Meteor. Climatol.,* **45,** 1388–1402.

Heymsfield, A. J., S. Matrosov, and B. Baum, 2003: Ice water path–optical depth relationships for cirrus and deep stratiform ice cloud layers. *J. Appl. Meteor.,* **42,** 1369–1390.

Inoue, T., 1987: A cloud type classification with *NOAA 7* split window measurements. *J. Geophys. Res.,* **92,** 3991–4000.

Karlsson, K.-G., 1996: Validation of modeled cloudiness using satellite-estimated cloud climatologies. *Tellus,* **48A,** 767–785.

Keil, C., A. Tafferner, H. Mannstein, and U. Schattler, 2003: Evaluating high-resolution model forecasts of European winter storms by use of satellite and radar observations. *Wea. Forecasting,* **18,** 732–747.

Klein, S. A., and C. Jakob, 1999: Validation and sensitivities of frontal clouds simulated by the ECMWF model. *Mon. Wea. Rev.,* **127,** 2514–2531.

Liu, Z., and Coauthors, 2008: CALIPSO lidar observations of the optical properties of Saharan dust: A case study of long-range transport. *J. Geophys. Res.,* **113,** D07207, doi:10.1029/2007JD008878.

Lopez, P., K. Finkele, P. Clark, and P. Mascart, 2003: Validation and intercomparison of three FASTEX cloud systems: Comparison with coarse-resolution simulations. *Quart. J. Roy. Meteor. Soc.,* **129,** 1841–1871.

Mathieu, A., G. Seze, C. Guerin, H. Dupais, and A. Weill, 1999: Mesoscale boundary layer cloud structures as observed during the SEMAPHORE campaign. *Phys. Chem. Earth,* **8B,** 933–938.

Mellor, G. L., and T. Yamada, 1982: Development of a turbulence closure model for geophysical fluid problems. *Rev. Geophys. Space Phys.,* **20,** 851–875.

Mlawer, E. J., S. J. Taubman, P. D. Brown, and M. J. Iacono, 1997: Radiative transfer for inhomogeneous atmospheres: RRTM, a validated correlated-*k* model for the longwave. *J. Geophys. Res.,* **102,** 16 663–16 682.

Norris, J. R., and C. P. Weaver, 2001: Improved techniques for evaluating GCM cloudiness applied to the NCAR CCM3. *J. Climate,* **14,** 2540–2550.

O'Dell, C. W., A. K. Heidinger, T. Greenwald, P. Bauer, and R. Bennartz, 2006: The successive-order-of-interaction radiative transfer model. Part II: Model performance and applications. *J. Appl. Meteor. Climatol.,* **45,** 1403–1413.

Otkin, J. A., and T. J. Greenwald, 2008: Comparison of WRF model-simulated and MODIS-derived cloud data. *Mon. Wea. Rev.,* **136,** 1957–1970.

——, D. J. Posselt, E. R. Olson, H.-L. Huang, J. E. Davies, J. Li, and C. S. Velden, 2007: Mesoscale numerical weather prediction models used in support of infrared hyperspectral measurements simulation and product algorithm development. *J. Atmos. Oceanic Technol.,* **24,** 585–601.

Prabhakara, C., R. S. Fraser, G. Dalu, M.-L. C. Wu, R. J. Curran, and T. Styles, 1988: Thin cirrus clouds: Seasonal distribution over oceans deduced from *Nimbus-4* IRIS. *J. Appl. Meteor.,* **27,** 379–399.

Rikus, L., 1997: Application of a scheme for validating clouds in an operational global NWP model. *Mon. Wea. Rev.,* **125,** 1615–1637.

Schmetz, J., P. Pili, S. Tjemkes, D. Just, J. Kerkmann, S. Rota, and A. Ratier, 2002: An introduction to Meteosat Second Generation (MSG). *Bull. Amer. Meteor. Soc.,* **83,** 977–992.

Schmit, T. J., M. M. Gunshor, W. P. Menzel, J. J. Gurka, J. Li, and A. S. Bachmeier, 2005: Introducing the next-generation Advanced Baseline Imager on GOES-R. *Bull. Amer. Meteor. Soc.,* **86,** 1079–1096.

Seeman, S. W., E. E. Borbas, R. O. Knuteson, G. R. Stephenson, and H.-L. Huang, 2008: Development of a global infrared land surface emissivity database for application to clear sky sounding retrievals from multispectral satellite radiance measurements. *J. Appl. Meteor. Climatol.,* **47,** 108–123.

Skamarock, W. C., J. B. Klemp, J. Dudhia, D. O. Gill, D. M. Barker, W. Wang, and J. G. Powers, 2005: A description of the Advanced Research WRF version 2. NCAR Tech. Note TN-468+STR, 88 pp.

Strabala, K. I., S. A. Ackerman, and W. P. Menzel, 1994: Cloud properties inferred from 8–12-μm data. *J. Appl. Meteor.,* **33,** 212–229.

Sun, Z., and L. Rikus, 2004: Validating model clouds and their optical properties using geostationary satellite imagery. *Mon. Wea. Rev.,* **132,** 2006–2020.

Thompson, G., P. R. Field, R. M. Rasmussen, and W. D. Hall, 2008: Explicit forecasts of winter precipitation using an improved bulk microphysics scheme. Part II: Implementation of a new snow parameterization. *Mon. Wea. Rev.,* **136,** 5095–5115.

Tselioudis, G., and C. Jakob, 2002: Evaluation of midlatitude cloud properties in a weather and a climate model: Dependence on dynamic regime and spatial resolution. *J. Geophys. Res.,* **107,** 4781, doi:10.1029/2002JD002259.

Westphal, D. L., and Coauthors, 1996: Initialization and validation of a simulation of cirrus using FIRE-II data. *J. Atmos. Sci.,* **53,** 3397–3429.

Yu, W., M. Doutriaux, G. Seze, H. Le Treut, and M. Desbois, 1996: A methodology study of the validation of clouds in GCMs using ISCCP satellite observations. *Climate Dyn.,* **12,** 389–401.

Zhang, Y., B. Rockel, R. Stuhlmann, R. Hollmann, and U. Karstens, 2001: REMO cloud modeling: Improvements and validation with ISCCP DX data. *J. Appl. Meteor.,* **40,** 389–408.